Environmental Research Communications

OPEN ACCESS

RECEIVED
3 January 2024

REVISED
31 March 2024

ACCEPTED FOR PUBLICATION
22 April 2024

PUBLISHED
7 May 2024

LETTER

Classified validation of Aeolus wind observations using IGRA over China

Shiyu Li[1,2], Yilun Chen[1,2], Zhaoyu Ou[1,2], Aoqi Zhang[1,2], Shumin Chen[1,2], Yong Han[1,2] and Weibiao Li[1,2]

[1] School of Atmospheric Sciences and Key Laboratory of Tropical Atmosphere-Ocean System, Ministry of Education, Sun Yat-sen University, Zhuhai, People's Republic of China
[2] Southern Marine Science and Engineering Guangdong Laboratory (Zhuhai), Zhuhai, People's Republic of China

E-mail: chenylun3@mail.sysu.edu.cn

Keywords: Aeolus, IGRA, wind validation

Supplementary material for this article is available online

Abstract

This study validated Aeolus wind observations over China from October 2020 to September 2022 using the Integrated Global Radiosonde Archive (IGRA). The results showed that most of the Aeolus observations were in good agreement with the IGRA observations. The quality of Aeolus Rayleigh-clear winds is superior to that of Mie-cloudy winds, and the wind products for ascending orbits are superior to those for descending orbits. The biases between Rayleigh-clear (Mie-cloudy) and IGRA winds are 0.61 (0.87), −0.01 (0.81), and 1.12 (1.59) m s^{-1} for the total, ascending and descending Aeolus orbits, respectively. Further classification study based on cloud height and relative humidity reveals that the quality of Mie-cloudy winds improves with cloud altitude until stratosphere, and Rayleigh-clear winds deteriorate for high relative humidity. The results provide a basis for quality control and error correction of Aeolus wind observations.

1. Introduction

The lack of direct measurements of wind profiles remains a major gap in the global observation system [1–3]. To overcome this deficiency, the European Space Agency (ESA) launched the Aeolus satellite mission in 2018, which carried the Atmospheric Laser Doppler Instrument (ALADIN) and became the first satellite mission to directly observe global wind profiles from space [4, 5]. The main objective of Aeolus is to use its profiles for data assimilation in numerical weather prediction (NWP) models, to improve the weather forecasts and advance the understanding of atmospheric dynamics [6, 7]. The benefits of assimilation of Aeolus wind profiles for NWP have been demonstrated, especially in the upper troposphere, lower stratosphere and tropical regions [8–10]. Therefore, it is imperative to characterize Aeolus data errors under various conditions to guide targeted quality control and calibration for optimization of NWP [7].

Aeolus wind products have been validated and compared with various reference data worldwide, including China [e.g., 11, 12, 13, 14]. The first validation of Aeolus wind products over China was conducted by Guo *et al* [11], who used ground-based radar wind profiler (RWP) observations to compare with the Level-2B (L2B) products. The R values (i.e., correlation coefficient) were 0.81 (0.94) between Rayleigh-clear (Mie-cloudy) and RWP winds. Wu *et al* [12] used ground-based coherent Doppler wind lidar to evaluate the Aeolus winds in the boundary layer and lower troposphere. They found that R value and bias (i.e., mean deviation) of Mie-cloudy winds were 0.83 and −0.25 m s^{-1}, while those of Rayleigh-clear winds were 0.62 and −1.15 m s^{-1}. However, due to the limited observation range of ground-based data, the validation work was only done for altitudes below 10 km.

Only a few aircraft and radiosondes have direct measurements in the lower stratosphere, while aircraft measurements are lacking in China [3]. Therefore, radiosondes are frequently used as reference data in Aeolus validation work [e.g., 3, 15, 16, 17, 18]. Using shipborne radiosonde data, Baars *et al* [3] evaluated the Aeolus wind products from 0 to 30 km over the Atlantic. They found that the Rayleigh-clear (Mie-cloudy) winds had systematic and random errors of 1.5 (1.0) m s^{-1} and 4.84 (1.58) m s^{-1}, respectively. Martin *et al* [13] compared radiosonde measurements and NWP forecast equivalents from two global models with Rayleigh-clear and Mie-cloudy winds from Aeolus. Biases were 1.4–2 m s^{-1} (Rayleigh) and 1.3–1.6 m s^{-1} (Mie) during ascending orbits, 1.6–2.3 m s^{-1} (Rayleigh) and 1.3–1.9 m s^{-1} (Mie) during descending orbits. Radiosondes have a wide and even distribution in China, and can directly measure pressure, temperature and relative humidity (RH) [19], which makes it convenient to do further classification studies for Aeolus verification work. Thus, the Integrated Global Radiosonde Archive (IGRA) is a suitable choice for reference data in China.

Most previous validation works only classified Aeolus L2B products according to geometric factors such as orbit, location, and time [11, 12, 16]. The impact of atmospheric physical conditions on the quality of Aeolus wind profiles remains unclear. We consider the different wind measurement principles of Mie-cloudy and Rayleigh-clear winds from Aeolus, and conduct classification studies on Aeolus wind products in two aspects [5, 20, 21]. On the one hand, Mie-cloudy winds are acquired from Mie backscatter signals induced by clouds, hence their quality varies depending on the cloud types. On the other hand, the retrieval algorithms of Rayleigh-clear winds imply that their quality is affected by the water vapor content in the air. In this paper, the quality of Aeolus L2B products over China is validated by comparing them with two years of IGRA wind observations (October 2020 to September 2022). We conduct a classification study on Mie-cloudy and Rayleigh-clear winds based on cloud types and RH respectively, in order to comprehensively analyze the quality of L2B products under various conditions. This paper aims to provide guidance for the application of Aeolus data, and offer insights for the planning of future similar satellite missions.

2. Data and methods

2.1. Aeolus wind observations

Aeolus flies in a sun-synchronous orbit with a height of approximately 320 km, and the orbit repeats its ground track every 7 days [4, 5, 22]. Aeolus is equipped with a 355-nm direct-detection wind lidar ALADIN, and uses the Doppler shift principle to obtain wind profiles of the horizontal line-of-sight (HLOS) component from the surface to 30 km altitude. The receiver has 24 vertical range bins with a vertical resolution of 0.25 to 2 km and a wind accuracy of 2 to 4 m s^{-1}, depending on altitude [6]. The HLOS wind speed is perpendicular to its orbit, with positive values for westerly winds on ascending orbits and negative values on descending orbits. ALADIN uses a dual-channel design, which can simultaneously obtain the particulate and molecular backscatter from Rayleigh and Mie channels. The L2B products provide Rayleigh-clear winds and Mie-cloudy winds. The former represent the winds observed in clear air (i.e., without aerosols and water/ice clouds), while the latter is the winds derived from the backscatter of aerosols or cloud particles [5].

The Aeolus dataset was released on May 12, 2020, and the L2B products have been entirely publicly accessible ever since. This study evaluates the Aeolus L2B products quality over China from October 2020 to September 2022 (baselines ranging from 2B11 to 2B14). This dataset was compared with temporally and spatially matched observations from IGRA. The auxiliary data, such as validity flag, estimated error, satellite azimuth angle, vertical center of gravity altitude, and top and bottom altitudes of the vertical bin, is also provided in the Aeolus L2B products. According to the official documents and previous studies, data quality is controlled by validity flags (0 for invalid, 1 for valid) and estimated errors. Following previous studies, only Rayleigh-clear and Mie-cloudy winds with a validity flag of 1 and estimated errors less than 8 m s^{-1} and 4 m s^{-1}, respectively, are selected [12, 16, 13].

2.2. IGRA wind observations

This study collected 00:00 and 12:00 UTC daily radiosonde observations over 237 stations in China from IGRA, comprising wind direction and speed, geopotential height, pressure, temperature, dewpoint temperature, RH, etc. All data underwent rigorous quality control [19]. Radiosonde measurements provide a reliable reference that other measurements can be verified against [23]. Sometimes, there are missing values in IGRA observations, and we used Gilbert's hypsometric formula and Lawrence's empirical RH formula to fill the missing geopotential height and RH values. The input data are pressure, temperature and dewpoint temperature from the same observation [24, 25].

2.3. Data matching procedures

Firstly, in order to compare IGRA and Aeolus wind observations, IGRA and Aeolus components need to be matched in time and space. Considering the fact that the rising speed of the radiosonde balloon is ~400 m min^{-1}, the time for the balloon to rise to 30 km is 75 min. If the average horizontal wind speed in the air is assumed to be 20 m s^{-1}, the horizontal displacement of the sounding balloon is 90 km. It is considered that the

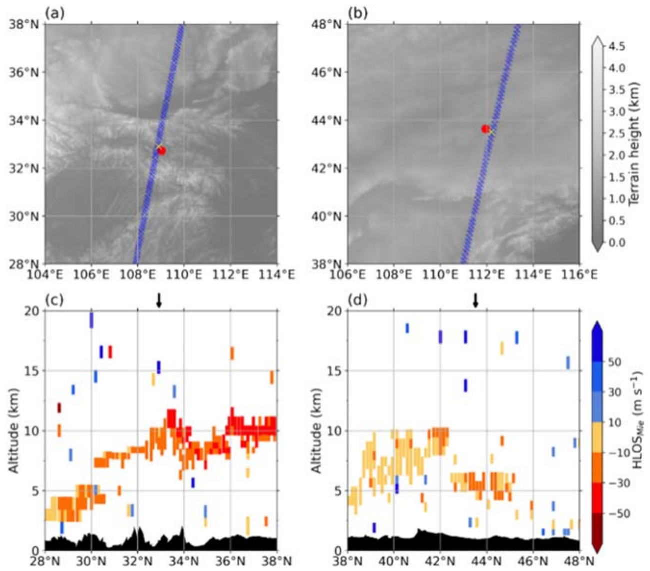

Figure 1. Station and orbit maps for case I and II (a), (b) and $HLOS_{Mie}$ distribution along latitude (c), (d). In a, a blue × is Aeolus orbit, a yellow × is matched station location, a red circle is IGRA station (Ankang). In b, same symbols for Erenhot station. In c and d, an arrow shows the wind profile matching IGRA. Aeolus measurement time for case I was 22:50 on Oct 7, 2020 (case II was 22:40 on May 18, 2022), while IGRA time was 0:00 the next day (Oct 8, 2020 and May 18, 2022).

wind speed does not change much within this range during the balloon-rising stage. Thus, this paper matches the Aeolus wind profiles with the IGRA wind profiles, requiring that the distance between Aeolus profile and IGRA station is not more than 100 km, and the matching time threshold is $\pm$ 1.5 h. The Aeolus observation that is closest to each IGRA observation in space is selected for comparison.

Moreover, After the spatiotemporal matching, altitude need to be matched. Vertically, each Aeolus profile acquires up to 24 range bins, with each range bin referred to as a sample. Similarly, each IGRA observation at every height is referred to as a sample. The L2B products provide top, center and bottom altitudes of the vertical bin. So, we require that the IGRA altitude fall within the top and bottom altitudes of the Aeolus range bin, and select the IGRA measurement with an altitude closest to the bin center altitude.

Finally, the IGRA samples that passed quality control and had non-missing wind direction and speed values need to be projected onto the HLOS wind direction [26]:

I. By using the detection principle and geometric relationship of radiosonde, the wind speed (w_s) and wind direction (w_d) measured by IGRA are converted to u and v wind components: $\begin{cases} u = w_s \times \cos(270^\circ - w_d) \\ v = w_s \times \sin(270^\circ - w_d) \end{cases}$

II. Then project the u, v wind components onto the HLOS direction:

$$HLOS_{IGRA} = -u\sin\varphi - v\cos\varphi$$

Where φ represents the azimuth angle of Aeolus. $HLOS_{IGRA}$ represents the value of the IGRA wind components projected onto the HLOS direction, while $HLOS_{Rayleigh}$ and $HLOS_{Mie}$ represent the Rayleigh-clear and Mie-cloudy winds respectively.

Thus, Rayleigh-clear (Mie-cloudy) acquired 8614 (1617) samples that matched with IGRA. To mitigate observational errors from IGRA and systematic errors from Aeolus, we have excluded samples with wind speeds exceeding $\pm$ 50 m s^{-1}. The resultant collocation dataset includes 8122 (Rayleigh-clear) and 1579 (Mie-cloudy) samples.

Figure 1 illustrates two case studies (case I, case II) comparing Mie-cloudy winds and IGRA winds, with overlaid terrain data from the National Oceanic and Atmospheric Administration (NOAA). Both cases correspond to the descending orbits. In Case I (figures 1(a), (c)), there are two Aeolus bins matching with radiosonde. At 8713 m above sea level, the $HLOS_{Mie}$ (-25 m s^{-1}) matches the $HLOS_{IGRA}$ (-21 m s^{-1}) showing a tiny westerly wind difference; but at 15269 m, the 69 m s^{-1} $HLOS_{Mie}$ is 69 m s^{-1} while the $HLOS_{IGRA}$ is -36 m s^{-1}, with a wind difference of 105 m s^{-1}. Despite consistent westerly $HLOS_{IGRA}$ aligning with actual observations, $HLOS_{Mie}$ presents an anomalously strong easterly wind. Case I demonstrates that the poor $HLOS_{Mie}$ quality at high altitudes. Case II (figures 1(b), (d)) shows decreases in wind differences (-14.9, 9, -0.1 m s^{-1}) across three matched bins (2352, 4620, 5376 m) between $HLOS_{Mie}$ and $HLOS_{IGRA}$. Preliminarily, Mie-cloudy wind quality improves with cloud altitude till stratosphere.

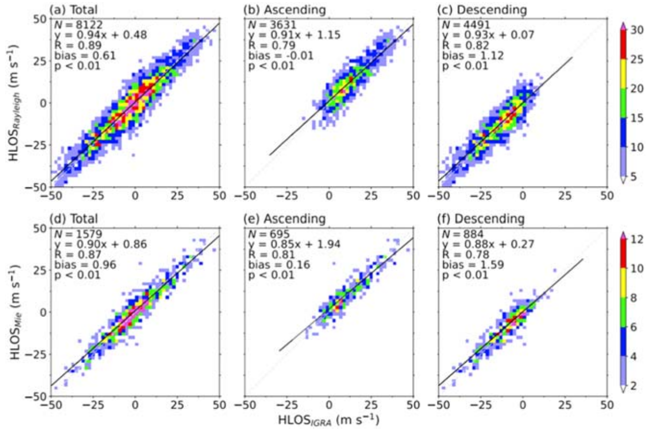

Figure 2. Two-dimensional histograms of IGRA HLOS winds versus Rayleigh-clear (a)–(c) and Mie-cloudy HLOS winds (d)–(f), with the total orbits (a), (d), ascending orbits (b), (e) and descending orbits (c), (f). The color shading represents frequency, with bin sizes $dx = dy = 2\ m\ s^{-1}$. The dashed line is the 1:1 line indicating $y = x$.

3. Results and discussion

As presented in figure 2, Rayleigh-clear (Mie-cloudy) acquired 3631 (695) and 4491 (884) samples matching with IGRA for the ascending and descending orbits. For Rayleigh-clear winds (figures 2(a)–(c)), the biases are 0.54, 0.19 and 0.82 m s^{-1} for the total, ascending and descending orbits, respectively. High correlation (0.89, 0.79, 0.82) at $p < 0.01$ level and ∼1 fitting slope indicate close Rayleigh-clear and IGRA wind agreements in China. Although also show relatively reliable quality, Mie-cloudy winds (figures 2(d)–(f)) exhibit a slightly lower quality versus Rayleigh-clear in terms of fitting slope, R and bias.

This conclusion conflicts the earlier research deeming that Mie-cloudy winds are more reliable [3, 11, 12]. This is because the Aeolus laser has aged, leading to a continuous decline in energy and weaker return signal. As a result, the random error has increased. Despite ESA promptly resetting N/P values since 2021 to improve Rayleigh-clear data quality by 15%, the error caused to Mie-cloudy winds remains non-negligible [27, 28]. Compared to Guo *et al* [12] yielding 2020 April-July RWP wind correlations of 0.81 (Rayleigh-clear) and 0.94 (Mie-cloudy), this study showcases quality rise in the former but decline in the latter.

Westerly winds dominate over China. As a result, wind speeds tend to be positive in ascending orbits and negative in descending orbits. For both Rayleigh-clear and Mie-cloudy winds, the R values are comparable between orbits, but bias favours ascending. Thus, the Aeolus wind quality is superior for ascending orbits, aligning with prior studies [11, 15]. Magnitude of bias between orbits is similar to a previous study [13].

Since Mie-cloudy winds are derived from Mie backscatter signals induced by clouds, their quality depends on the cloud types [20, 29, 30]. Based on meteorological definitions, Mie-cloudy winds detected in clouds below 2.5 km are classified as low cloud winds, those between 2.5 and 6 km as middle cloud winds, those between 6 and 14 km as high cloud winds, and above 14 km as stratospheric cloud winds [31]. Thus, wind samples are classified into four types for the scatterplots of $HLOS_{Mie}$ versus $HLOS_{IGRA}$ (figure 3): low clouds (264 samples), middle clouds (483), high clouds (778), and stratospheric clouds (54). Respective linear fit slopes (R values) are 0.77 (0.48), 0.88 (0.78), 0.92 (0.95), and 0.36 (0.33), with R values being significant at $p < 0.01$ level except those of stratospheric clouds. The biases of each type are 0.77, 1.16, 0.56, and 5.89 m s^{-1}. Apart from the lower bias in low clouds due to weaker winds, the quality of Mie-cloudy winds improves with cloud altitude from low to high clouds but is poor for stratospheric clouds.

On the one hand, the quality of tropospheric Mie-cloudy winds improved with cloud altitude. This matches other validation studies [17]. This is likely because lower clouds contain more water vapor, aerosols, and hydrometeors such as precipitation which reduce the signal-to-noise ratio of the Mie channel [32, 33]. These substances strongly scatter and reflect UV light, heavily attenuating Mie-cloudy wind signals in lower clouds. In contrast, their concentrations are lower in middle and high clouds, resulting in less interference and thus better quality with altitude [32]. Alternatively, some studies attribute the poor quality of low cloud winds to additional path attenuation, as the laser beam has to travel farther to reach the lower clouds and return to the receiver [5, 21].

On the other hand, winds in stratospheric clouds (above 14 km) have poor quality due to their unique properties. They comprise the strongly developed cumulonimbus tops and spreading cirrus clouds [31]. The inhomogeneous, multi-layered cirrus clouds reduce the signal quality through non-uniform filling effects

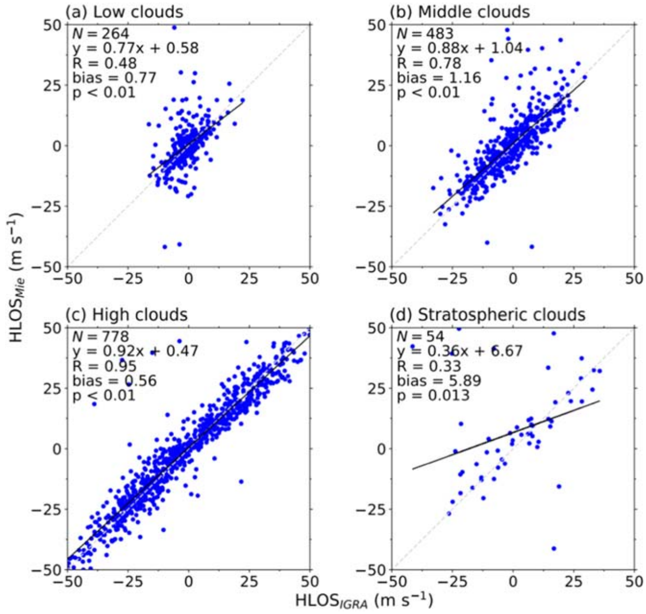

Figure 3. Scatterplots of $HLOS_{Mie}$ versus $HLOS_{IGRA}$ for (a) low clouds below 2.5 km, (b) middle clouds at 2.5–6 km, (c) high clouds at 6–1.4 km, and (d) stratospheric clouds above 1.4 km. The dashed line is the 1:1 line indicating $y = x$.

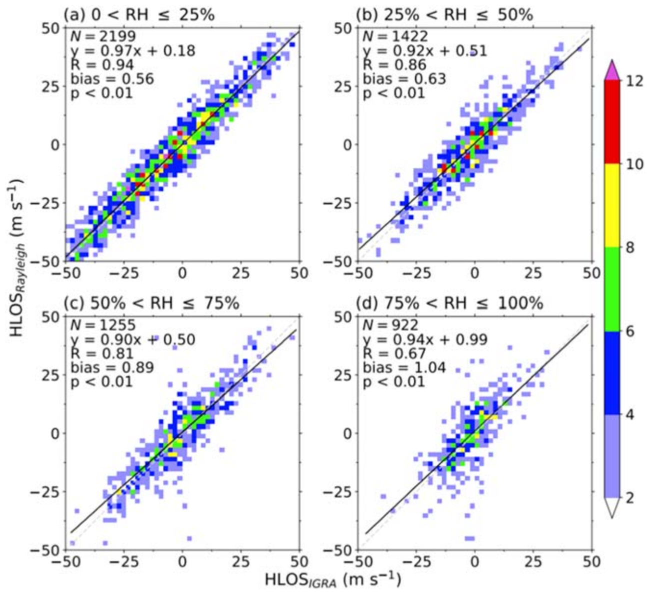

Figure 4. Two-dimensional histograms comparing $HLOS_{Rayleigh}$ and $HLOS_{IGRA}$ winds at different relative humidity (RH) levels. The color shading represents frequency, with bin sizes of $dx = dy = 2\ m\ s^{-1}$. The dashed line is the 1:1 line indicating $y = x$.

[30, 33]. Additionally, complex winds with entrainment occur near cumulonimbus tops. These winds degrade signals through Doppler shifts, which are also observed by CALIPSO [21, 29, 30].

To analyse further, we exclude samples with missing RH data from IGRA. Then we classify Rayleigh-clear winds into four RH levels, with 2199, 1422, 1255, and 922 samples each (figure 4). The R (bias) values decrease (increase) with increasing RH: 0.94 (0.56 m s^{-1}), 0.86 (0.63 m s^{-1}), 0.81 (0.89 m s^{-1}), and 0.67 (1.04 m s^{-1}), all R values significant at $p < 0.01$ level. This means that the quality of Rayleigh-clear winds deteriorated at high RH.

This is probably because Rayleigh-clear winds are calculated based on Doppler shifts under a dry air assumption, excluding water vapor and aerosols. Water vapor in the air substantially absorbs and scatters UV radiation, altering Doppler shifts at high RH. This impacts wind retrieval by deviating from the dry air conditions assumed [5, 21, 34].

Besides, higher altitudes usually exhibit lower RH levels, thus the influence of altitude should be excluded when discussing the impact of RH on wind quality. The altitude peak count of samples decreases with increasing

RH levels (as shown in figure S1). We have selected samples within the 4—6 km altitude range to compare $HLOS_{Rayleigh}$ with $HLOS_{IGRA}$ winds (as depicted in figure S2). After eliminating the impact of altitude, the findings still support the previous conclusion.

4. Conclusions

Aeolus provides the first global profile observations. Validation of Aeolus wind products is necessary. This study collected Aeolus L2B products from October 2020 to September 2022, and verified them with spatially and temporally matched wind observations from IGRA. The need for evaluating the quality of Aeolus products in the stratosphere, as argued by Bley *et al* [18] and Chen *et al* [14], is reflected in this study.

Statistical analyses of linear fit slopes, R values, and biases indicate that the Aeolus L2B products and IGRA observations agree well overall. Rayleigh-clear winds outperform Mie-cloudy winds, which can be attributed to data correction after 2021. Both wind products exhibit superior quality in ascending over descending orbits. Classification studies by cloud types and RH reveal that Mie-cloudy winds quality betters with cloud altitude till stratosphere, while Rayleigh-clear worsens at high RH [20, 21, 30].

Leveraging the unique measurement principles of Aeolus and IGRA's capability for direct RH observations, this study innovatively classified Mie-cloudy and Rayleigh-clear winds to analyse the quality of Aeolus wind products under various conditions. The insights on the impacts of cloud types and RH on wind lidar quality provide a basis for Aeolus data quality control and error correction, and inform future spaceborne wind lidar developments. Due to the spatiotemporal resolution limitations of the radiosondes and Aeolus, the matching thresholds used herein were constrained. Therefore, future verification with higher resolution observations is needed to validate the conclusions.

Acknowledgments

This study was jointly supported by the National Basic Research and Development Project of China (2022YFF0802000), the National Natural Science Foundation of China (grant numbers 42105068, 42075004, 42027804 and 41775026), the Guangdong Basic and Applied Basic Research Foundation (grant numbers 2023A1515240045), and the Innovation Group Project of Southern Marine Science and Engineering Guangdong Laboratory (Zhuhai) (grant number 311022006).

Data availability statement

All data that support the findings of this study are included within the article (and any supplementary files).

Open research

The IGRA data used in this paper can be downloaded form https://.ncei.noaa.gov/data/integrated-global-radiosonde-archive/access/data-por/. The Aeolus data were provided by the European Space Agency (ESA), and can be accessed via https://aeolus-ds.eo.esa.int/oads/access/.

ORCID iDs

Shiyu Li https://orcid.org/0009-0005-1945-3063

References

[1] Weissmann M and Cardinali C 2007 Impact of airborne doppler lidar observations on ECMWF forecasts *Q. J. R. Meteorolog. Soc.* **133** 107–16
[2] Illingworth A J *et al* 2018 WIVERN: a new satellite concept to provide global in-cloud winds, precipitation, and cloud properties *Bull. Am. Meteorol. Soc.* **99** 1669–87
[3] Baars H *et al* 2020 Validation of Aeolus wind products above the Atlantic Ocean *Atmos. Meas. Tech.* **13** 6007–24
[4] Ingmann P 1999 The four candidate Earth Explorer core missions. Report for mission selection. 4. Atmospheric Dynamics Mission. ESA. (Available at: https://cimss.ssec.wisc.edu/iwwg/iww5/S6-3_Ingmann-TheAtmospheric.pdf, last access: 29 April 2024)
[5] Reitebuch O 2012 The spaceborne wind lidar mission ADM-Aeolus *Atmospheric Physics: Background – Methods – Trends* ed Heidelberg Berlin (Springer) 815–827
[6] Lux O *et al* 2020 High-power and frequency-stable ultraviolet laser performance in space for the wind lidar on Aeolus *Opt. Lett.* **45** 1443–6

[7] Rennie M *et al* 2021 Demonstrated Aeolus benefits in atmospheric sciences *2021 IEEE Int. Geoscience and Remote Sensing Symp. IGARSS.* (https://doi.org/10.1109/IGARSS47720.2021.9554267)
[8] Horányi A, Cardinali C, Rennie M and Isaksen L 2015 The assimilation of horizontal line-of-sight wind information into the ECMWF data assimilation and forecasting system: I. The assessment of wind impact *Q. J. R. Meteorolog. Soc.* **141** 1223–32
[9] Zagar N, Rennie M and Isaksen L 2021 Uncertainties in Kelvin Waves in ECMWF analyses and forecasts: insights from Aeolus observing system experiments *Geophys. Res. Lett.* **48** e2021GL094716
[10] Mile M, Azad R and Marseille G-J 2022 Assimilation of Aeolus rayleigh-clear winds using a footprint operator in AROME-Arctic Mesoscale model *Geophys. Res. Lett.* **49** e2021GL097615
[11] Guo J *et al* 2021 Technical note: first comparison of wind observations from ESA's satellite mission Aeolus and ground-based radar wind profiler network of China *Atmos. Chem. Phys.* **21** 2945–58
[12] Wu S *et al* 2022 Inter-comparison of wind measurements in the atmospheric boundary layer and the lower troposphere with Aeolus and a ground-based coherent Doppler lidar network over China *Atmos. Meas. Tech.* **15** 131–48
[13] Witschas B *et al* 2020 First validation of Aeolus wind observations by airborne doppler wind lidar measurements *Atmos. Meas. Tech.* **13** 2381–96
[14] Chen C *et al* 2022 Comparison of lower stratosphere wind observations from the USTC's rayleigh doppler lidar and the ESA's satellite mission Aeolus *Earth and Space Science* **9** e2021EA002176
[15] Martin A *et al* 2021 Validation of Aeolus winds using radiosonde observations and numerical weather prediction model equivalents *Atmos. Meas. Tech.* **14** 2167–83
[16] Chen S *et al* 2021 Study of the seasonal variation in Aeolus wind product performance over China using ERA5 and radiosonde data *Atmos. Chem. Phys.* **21** 11489–504
[17] Rani S I *et al* 2022 Assessing the quality of novel Aeolus winds for NWP applications at NCMRWF *Q. J. R. Meteorolog. Soc.* **148** 1344–67
[18] Bley S *et al* 2022 Validation of the Aeolus L2B Rayleigh winds and ECMWF short-range forecasts in the upper troposphere and lower stratosphere using loon super pressure balloon observations *Q. J. R. Meteorolog. Soc.* **148** 3852–68
[19] Durre I, Yin X G, Vose R S, Applequist S and Arnfield J 2018 Enhancing the data coverage in the integrated global radiosonde archive *J. Atmos. Oceanic Technol.* **35** 1753–70
[20] Flament T *et al* 2021 Aeolus L2A aerosol optical properties product: standard correct algorithm and Mie correct algorithm *Atmos. Meas. Tech.* **14** 7851–71
[21] Reitebuch O *et al* 2009 The airborne demonstrator for the direct-detection doppler wind lidar ALADIN on ADM-Aeolus: I. Instrument design and comparison to satellite instrument *J. Atmos. Oceanic Technol.* **26** 2501–15
[22] Lolli S, Delaval A, Loth C, Garnier A and Flamant P H 2013 0.355-micrometer direct detection wind lidar under testing during a field campaign in consideration of ESA's ADM-Aeolus mission *Atmos. Meas. Tech.* **6** 3349–58
[23] Bony S *et al* 2017 EUREC4A: a field campaign to elucidate the couplings between clouds, convection and circulation *Surv. Geophys.* **38** 1529–1568
[24] Gilbert G K 1882 *A New Method of Measuring Heights by Means of the Barometer Washington* ed L David (US Government Printing Office)
[25] Lawrence M G 2005 The relationship between relative humidity and the dewpoint temperature in moist air: a simple conversion and applications *Bull. Am. Meteorol. Soc.* **86** 225–34
[26] Rennie M P *et al* 2021 The impact of Aeolus wind retrievals on ECMWF global weather forecasts *Q. J. R. Meteorolog. Soc.* **147** 3555–86
[27] Rennie M *et al* 2022 NWP monitoring of L2B product quality at ECMWF[EB/OL](Tech. Rep.). ECMWF. (Available at: https://az659834.vo.msecnd.net/eventsairwesteuprod/production-nikal-public/f15539060d4c46b9b8fff61d8c7a303a, last access: 29 April 2024)
[28] Hu Z and Bu L 2023 Review of the progress of Aeolus space-borne wind measurement lidar *Infrared and Laser Engineering* **52** 20220691
[29] Vaughan M A, Winker D M and Powell K A 2005 CALIOP Algorithm Theoretical Basis Document, part 2, Feature detection and layer properties algorithms, PC-SCI-202.01, NASA Langley Res. Cent., (available at: https://www-calipso.larc.nasa.gov/resources/pdfs/PC-SCI-202_Part2_rev1x01.pdf, last access: 29 April 2024).
[30] Hu Y *et al* 2007 The depolarization - attenuated backscatter relation: CALIPSO lidar measurements vs. theory *Opt. Express* **15** 5327–32
[31] WMO 1987 Manual on the observation of clouds and other meteors(Tech. Rep). ECMWF. (Available at: https://cloudatlas.wmo.int/docs/wmo_407_en-v1.pdf, last access: 29 April 2024)
[32] Lebsock M and Su H 2014 Application of active spaceborne remote sensing for understanding biases between passive cloud water path retrievals *Journal of Geophysical Research: Atmospheres* **119** 8962–79
[33] Flamant P H *et al* 2020 ADM-Aeolus L2A algorithm theoretical baseline document, particle spin-off products, Tech. Rep., ESA. (Available at: https://earth.esa.int/eogateway/catalog/aeolus-l2a-aerosol-cloud-optical-product)
[34] Dabas A *et al* 2008 Correcting winds measured with a rayleigh doppler lidar from pressure and temperature effects *Tellus A: Dynamic Meteorology and Oceanography* **60** 206–15